Titre: Title:	Assessing therapeutic response non-invasively in a neonatal rat model of acute inflammatory white matter injury using high-field MRI
Auteurs: Authors:	Wyston C. Pierre, Luis Akakpo, Irène Londono, Philippe Pouliot, Sylvain Chemtob, Frédéric Lesage, & Gregory A. Lodygensky
Date:	2019
Type:	Article de revue / Article
Référence: Citation:	Pierre, W. C., Akakpo, L., Londono, I., Pouliot, P., Chemtob, S., Lesage, F., & Lodygensky, G. A. (2019). Assessing therapeutic response non-invasively in a neonatal rat model of acute inflammatory white matter injury using high-field MRI. Brain, Behavior, and Immunity, 81, 348-360. https://doi.org/10.1016/j.bbi.2019.06.032

Document en libre accès dans PolyPublie
Open Access document in PolyPublie

| **URL de PolyPublie:** PolyPublie URL:	https://publications.polymtl.ca/5087/
Version:	Version officielle de l'éditeur / Published version Révisé par les pairs / Refereed
Conditions d'utilisation: Terms of Use:	CC BY-NC-ND

Document publié chez l'éditeur officiel
Document issued by the official publisher

Titre de la revue: Journal Title:	Brain, Behavior, and Immunity (vol. 81)
Maison d'édition: Publisher:	Elsevier
URL officiel: Official URL:	https://doi.org/10.1016/j.bbi.2019.06.032
Mention légale: Legal notice:	
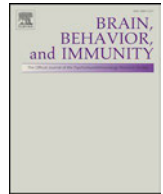
Assessing therapeutic response non-invasively in a neonatal rat model of acute inflammatory white matter injury using high-field MRI

Wyston C. Pierre[a,b], Luis Akakpo[a,c], Irène Londono[a], Philippe Pouliot[c,d], Sylvain Chemtob[a,b,e], Frédéric Lesage[c,d], Gregory A. Lodygensky[a,b,d,*]

[a] Departments of Pediatrics, Ophthalmology and Pharmacology, CHU Sainte-Justine Research Centre, Montréal, Canada
[b] Department of Pharmacology, Université de Montréal, Montréal, Canada
[c] École Polytechnique de Montréal, Montreal, QC, Canada
[d] Montreal Heart Institute, Montreal, QC, Canada
[e] Department of Pharmacology and Therapeutics, McGill University, Montréal, Canada

ARTICLE INFO

ABSTRACT

Perinatal infection and inflammatory episodes in preterm infants are associated with diffuse white matter injury (WMI) and adverse neurological outcomes. Inflammation-induced WMI was previously shown to be linked with later hippocampal atrophy as well as learning and memory impairments in preterm infants. Early evaluation of injury load and therapeutic response with non-invasive tools such as multimodal magnetic resonance imaging (MRI) would greatly improve the search of new therapeutic approaches in preterm infants. Our aim was to evaluate the potential of multimodal MRI to detect the response of interleukin-1 receptor antagonist (IL-1Ra) treatment, known for its neuroprotective properties, during the acute phase of injury on a model of neonatal WMI.

Rat pups at postnatal day 3 (P3) received intracerebral injection of lipopolysaccharide with systemic IL-1Ra therapy. 24 h later (P4), rats were imaged with multimodal MRI to assess microstructure by diffusion tensor imaging (DTI) and neurochemical profile of the hippocampus with ^{1}H-magnetic resonance spectroscopy. Astrocyte and microglial activation, apoptosis and the mRNA expression of pro-inflammatory and necroptotic markers were assessed.

During the acute phase of injury, neonatal LPS exposure altered the concentration of hippocampus metabolites related to neuronal integrity, neurotransmission and membrane integrity and induced diffusivity restriction. Just 24 h after initiation of therapy, early indication of IL-1Ra neuroprotective effect could be detected *in vivo* by non-invasive spectroscopy and DTI, and confirmed with immunohistochemical evaluation and mRNA expression of inflammatory markers and cell death.

In conclusion, multimodal MRI, particularly DTI, can detect not only injury but also the acute therapeutic effect of IL-1Ra suggesting that MRI could be a useful non-invasive tool to follow, at early time points, the therapeutic response in preterm infants.

1. Introduction

More than 50% of very low birth weight (VLBW) preterm infants are affected by white matter injury (WMI) (Volpe, 2009; Pavlova and Krageloh-Mann, 2013). Magnetic resonance imaging (MRI) allows the detection of diffusive WMI in up to 79% of preterm infants (Maalouf et al., 2001). Perinatal inflammation and infection (from chorioamniotis, necrotizing enterocolitis, sepsis and sustained ventilation) are major risk factors of WMI (Khwaja and Volpe, 2008). Together with hypoxic-ischemic injuries, inflammatory injuries are the main pathogenic factors in periventricular leukomalacia (PVL) (Khwaja and Volpe, 2008). The diagnosis is usually confirmed at the end of the hospitalization by imaging. In the months following discharge, physical and occupational therapies are then introduced if found clinically relevant. To date, there is no recognized therapy to treat WMI at the earliest onset. With the advancements in non-invasive imaging tools, the question that comes to mind is if an early recognition of on-going WMI by imaging could trigger the application of a therapy and if its effect

could then be monitored.

A robust animal model of inflammatory WMI, consisting in the injection of lipopolysaccharides (LPS) in the corpus callosum of rat pups, was shown to reproduce the pathophysiological hallmarks seen in preterm infants with WMI such as microglia activation, astrogliosis, ventricular dilatation and hypomyelination (Cai et al., 2003; Pang et al., 2003; Lodygensky et al., 2010). This animal model showed several neurobehavioral alterations, observed in preterm infants with WMI, which includes hyperactivity, memory impairments and motor deficits (Fan et al., 2008b; Khwaja and Volpe, 2008; Volpe, 2009; Fan et al., 2011; Wang et al., 2013; Back and Rosenberg, 2014). Furthermore, late hippocampal atrophy following preterm birth exacerbated by WMI is also reproduced in this model (Fan et al., 2005; Lodygensky et al., 2005; Fan et al., 2008a; Thompson et al., 2008). An up-regulation of pro-inflammatory cytokines associated to adverse neurodevelopmental outcomes in preterm infants was also seen in this model, which includes interleukin-6 (IL-6), tumor necrosis factor alpha (TNF-α) and, long-lasting elevated levels of interleukin-1β (IL-1β) (Pang et al., 2003; Lodygensky et al., 2014; Jin et al., 2015; Galinsky et al., 2018). Particularly, clinical and animal studies in WMI suggest that IL-1β plays a central role in the acute and chronic phase of injury (Girard et al., 2010; Favrais et al., 2011; Rosenzweig et al., 2014). Compared to IL-6 and TNF-α, exposure to IL-1β alone in neonatal animals resulted in a more severe neuropathological phenotype characterized by microglial activation, increased cell death, oligodendrocytes impairments and behavioral alterations (Lee et al., 1993; Pang et al., 2003; Cai et al., 2004; Pang et al., 2006). The study of Girard et al. demonstrated that acute phase of WMI in preterm infants was characterized by an increased expression of IL-1β and IL-1 receptor, with no expression of its natural antagonist the IL-1 receptor antagonist (IL-1Ra) (Girard et al., 2010). As mentioned earlier, there is currently no approved therapeutic drug in inflammatory WMI but human recombinant IL-1Ra is an interesting therapeutic target with promising neuroprotective potential that was approved by the FDA in 2013 in the pediatric population to treat neonatal-onset multisystem inflammatory disease (Dinarello et al., 2012; Rosenzweig et al., 2014). In the LPS-induced WMI model described earlier, simultaneous intracerebral injection of IL-1Ra (but not with TNF-α antibody) decreased the extent of LPS-induced injury (Cai et al., 2003; Pang et al., 2003). Furthermore, systemic administration of IL-1Ra protected against brain injury in models of perinatal systemic inflammation (Girard et al., 2012; Savard et al., 2013; Savard et al., 2015).

Recent amelioration in neonatal intensive care led to a decrease in cystic PVL which made diffuse WMI such as non-cystic PVL the most common WMI in preterm infants (Khwaja and Volpe, 2008). Compared to cystic PVL, diffuse WMI cannot be identified reliably by ultrasonography as its cystic counterpart (Inder et al., 2003). In the study of Inder et al., on a 30 weeks born preterm, the use of diffusion weighted imaging was able to detect early signs of injury (5 days post birth), with widespread apparent diffusion coefficient reduction in the white matter at a time where ultrasonography and traditional MRI did not detect any changes (Inder et al., 1999). This sharp decrease in diffusivity seen on mean diffusivity maps (MD) occurs during the first few days following brain injury and was initially described in patients with stroke and in newborns with birth asphyxia (McKinstry et al., 2002). In rat pups injected with LPS intracerebrally, MD restriction detected *in vivo* has been shown to strongly correlate with apoptosis in the corpus callosum (Lodygensky et al., 2014). In rat pups, MRS detected metabolic changes identical to preterm infants with white matter injury showing an increased concentration of lactate and macromolecules in the corpus callosum 24 h following the LPS injection (Lodygensky et al., 2014). In a clinical setting, *in vivo* MRI (DTI and MRS) was able to monitor early therapeutic response in different diseases including glioblastoma (Najac and Ronen, 2016; Price et al., 2016), breast cancer (Bathen et al., 2011; Sharma et al., 2011; Cao et al., 2012), strokes (Schabitz and Fisher, 1995; Seitz and Donnan, 2010), and depression (Caverzasi et al., 2012).

The aim of this paper was to demonstrate, in rat pups, the use of magnetic resonance technologies (DTI and MRS) as potential tools for *in vivo* monitoring of therapeutic response to IL-1Ra following LPS exposure.

2. Methods

2.1. Animal preparation

Sprague-Dawley dams and their litter composed of male rats at one day of life (P1) were obtained from Charles River Laboratories (Charles River, Canada). They were allowed to acclimatize to the animal facility prior to experimental procedures. The animals had free access to water and food and were exposed to 12 h light/dark cycles. All animal-handling procedures were approved by the Institutional Committee for Animal Care of the Montreal Heart Institute Research Center, following the recommendations of the Canadian Council of Animal Care.

2.1.1. Intracerebral injection

Forty-eight 3 days old (P3) male Sprague-Dawley rats (average weight of 8.77 $\pm$ 0.09 g) were randomly assigned to one of three experimental groups: Sham (n = 17), LPS (n = 16) and LPS + IL-1Ra (n = 15); with each litter having at least 2 animals from each treatment group. LPS exposed animals received an intracerebral injection of a suspension of 16 µg/µL LPS (1 mg/kg; Lipopolysaccharide E. coli, serotype 055:B5; SigmaAldrich, Oakville, ON, Canada), in sterile saline (0.5 µL for 8 g pup) and, Sham pups received an equivalent volume of 0.9% sterile saline solution alone. The intracerebral injection was made in the corpus callosum at a level equivalent to P-7, c9 (Ramachandra and Subramanian, 2011) under ultrasound guidance using Vevo LAZR micro-ultrasound system (FUJIFILM VisualSonics Inc., Toronto, ON, Canada) as it was previously published (Lodygensky et al., 2014). A micropipette mounted on a microprocessor-controlled injector (Micro4 from World Precision Instruments, Sarasota, FL, USA) with a rate of 100 nL/min was used for the injections. All the intracerebral injections were performed under isoflurane anaesthesia.

2.1.2. Animal treatment

LPS animals were further divided into two groups: one with IP injection of IL-1Ra (LPS + IL-1Ra; 2 mg/kg; Kineret-Anakinra, Amgen, Thousand Oaks, CA, USA) and the other with IP injection of 0.9% sterile saline (LPS). Doses were administered at 5 min, 6 h and 22–24 h after intracerebral LPS injection. Half of the animals (n = 24) were imaged at MRI, euthanized and the brains were collected for immunohistochemistry. For the other half (n = 24), MRI was not performed, pups were euthanized, and the brains were collected for biochemical and gene expression analysis.

2.2. Nuclear magnetic resonance

Animals were anaesthetized by isoflurane (3% for induction; 0.5–2% for maintenance) in a mixture of 0.25% air and 0.5% O_2 and placed in a tailor-made MRI-compatible ertalyte head-holder. The procedure was performed according to previously described protocols (Lodygensky et al., 2014). Physiology monitoring was conducted with a custom-built pressure pillow combined with a temperature probe placed under the abdomen. Temperature was maintained stable at 36 °C. Respiration was maintained between 50 and 100 breaths/min by adapting the level of isoflurane. Imaging and spectroscopy acquisitions were conducted using a specifically designed quadrature surface coil consisting of two geometrically decoupled loops of 14 mm in diameter. All MRI/MRS experiments were acquired on an actively shielded 7-T/30-cm horizontal bore magnet scanner interfaced with a DirectDrive console (Agilent, Palo Alto, CA, USA) with gradients of 600 mT/m.

2.2.1. Diffusion Tensor Imaging (DTI)

Diffusion-weighted images were acquired with a coronal-plane resolution of $117 \times 234 \, \mu m^2$ and a slice thickness of $600 \, \mu m$. Data was acquired using a standard spin echo sequence (repetition time = 2.2 s and an echo time = 35 ms) with an origin-symmetric diffusion gradient direction (2×6) and b-values of 0 and $700 \, s/mm^2$ similarly to our study using this animal model (Lodygensky et al., 2010). The diffusion-weighting gradients were applied for a duration (∂) of 7 ms and a delay (Δ) of 21 ms with 4 averages and a total scan time of 1 h.

2.2.1.1. DTI analysis. The diffusion tensor was fitted to the diffusion-weighted data (weighted linear least square) and different scalar maps were extracted from the tensor. Fractional anisotropy (FA), radial diffusivity (RD), axial diffusivity (AD), mean diffusivity (MD) and color-coded (Red, Green and Blue - RGB) FA maps were derived from the diffusion tensor using a software written in Matlab (MathWorks, Natick, MA, USA) developed by Song et al. (Song et al., 2002; Song et al., 2003; Sun et al., 2003; Song et al., 2005). The color-coded FA map was used as principal view for the positioning of regions of interest (ROIs), as it offers a greater contrast between white and grey matter, but the placement was validated with the other scalar maps. The ROIs were positioned by a rater (L.A.) on the corpus callosum and on ipsilateral and contralateral cingulum, as labeled by Paxinos and Watson atlas (Paxinos and Watson, 2007), on three consecutive slices at a level equivalent to P-1, c7 and P-1,c10 (Ramachandra and Subramanian, 2011). The ROIs were drawn using NIH's ImageJ software and for each slice, the mean of the ROIs was measured on the FA, RD, AD and MD maps as previously published (Lodygensky et al., 2010; Lodygensky et al., 2014).

2.2.2. Magnetic resonance spectroscopy

Anatomical images were acquired to allow the positioning of the volumes of interest (VOI) for the spectroscopy experiments. They were obtained with a fast spin echo MRI sequence (repetition time = 3 s, echo train length = 8, effective echo time = 78 ms) with an in-plane resolution of $58 \times 117 \, \mu m^2$ and a slice thickness of $600 \, \mu m$ and a total scan time of 5 min. The VOIs were placed on the ipsilateral hippocampus known to have an impaired growth following LPS exposure (VOI = $1.5 \times 3 \times 2 \, mm^3$). The B_0 magnetic field homogeneity was adjusted using FASTMAP (Gruetter, 1993). Localized spectra were acquired with SPECIAL sequence using a very short echo time (2.7 ms) combined with water suppression and an outer volume suppression as described previously (Mlynarik et al., 2006; Lodygensky et al., 2014). The spectra were acquired in 18 blocks of 16 to improve signal-to-noise ratio, a bandwidth of 5 kHz, 4096 complex data points and a repetition time of 4 s, for a total acquisition time of 19 min. An additional spectrum with an unsuppressed water signal was acquired for referencing and eddy-current correction.

2.2.2.1. MRS analysis. Spectra were post-processed using an in-house MATLAB pipeline before the metabolite quantification using the LCModel (Provencher, 1993). FIDs were corrected for the phase and frequency shifts between the blocks of the spectra, due to the B_0 magnetic field drift in time, as described in (Near et al., 2015). All blocks were then summed together to increase the SNR, a DC offset correction and a left shift of the 4 first complex data points were also

applied to minimize the first-order phase error. All these steps were conducted using the FID-A matlab toolbox (Simpson et al., 2017). The following 18 metabolites were quantified using LCModel: alanine (Ala), aspartate (Asp), creatine (Cr), γ-aminobutyric acid (GABA), glucose (Glc), glutamate (Glu), glutamine (Gln), glycine (Glyc), glutathione (GSH), glycerophosphorylcholine (GPC), phosphorylcholine (PCh), myo-inositol (Ins), lactate (Lac), N-acetylaspartate (NAA), N-acetylaspartylglutamate (NAAG), phosphocreatine (PCr), phosphoethanolamine (PE) and taurine (Tau). In addition to these, lipids and macromolecules signals at specific chemical-shifts were also considered as targets for the search of a biomarker and were studied in the same way as the aforementioned molecules.

Only metabolite with a Cramer-Rao lower bound inferior to 20 were kept. A limit on linewidth (30 Hz maximum) and SNR (5 minimum) was also applied.

2.3. Tissue preparation for immunohistochemistry

Following the MRI, the rats were deeply anaesthetized with isoflurane and transcardially perfused with saline followed by 4% paraformaldehyde (PFA). Brains were extracted and submerged in 4% PFA for 24 h at 4 °C and then cryoprotected by immersion in 30% sucrose for at least 48 h. Brains were kept at 4 °C until cutting. Coronal sections (50 μm thick) were cut on a cryostat and conserved at − 20 °C in cryoprotectant solution (30% ethylene glycol in 0.03 mol/L PBS and 15% sucrose) until staining. Special care was taken to ensure that the midline of the brain was absolutely perpendicular to the blade for cutting coronal sections.

2.3.1. Immunohistochemistry

Immunohistochemistry was performed on five free-floating brain sections, 300 μm apart, for each animal using the antibodies listed in Table 1 to evaluate cell death (fractin), microgliosis (Iba-1) and astrogliosis (GFAP). Briefly, the selected cryosections were washed in PBS and, transferred to blocking buffer (1% BSA, 1–5% normal goat serum (NGS), 0.3% Triton X100) for 2 h with gentle agitation. Sections were then incubated in the primary antibody solution prepared with diluent buffer (1% BSA, 0.1% Triton X100 and 1% NGS) at 4 °C overnight with gentle agitation. The day after, sections were washed in PBS and incubated for 2 h at room temperature in the secondary antibody solution prepared in diluent buffer. At the end, sections were washed in PBS, stained with PureBlu DAPI solution (0.074% in PBS; Bio-Rad, Mississauga, ON, Canada) for 5 min, washed in PBS and mounted on gelatin-coated slides. Slides were air-dried and mounted with Fluorogel (EMS, Cedarlane Labs, Burlington, ON, Canada) before scanning them at $20\times$ in the slide scanner Axioscan Z1 (Zeiss, Toronto, ON, Canada).

2.3.2. Immunohistochemistry analysis

ROIs with fixed dimension (2000×1000 pixels) were drawn out the AxioScan whole brain images and quantified using ImageJ. For the quantification, a pixel intensity threshold was defined as the non-specific background noise intensity as seen on the control brain slices incubated solely with the Alexa488 secondary antibody. For the particulated labeling of fractin, the number of Fractin[+] pixels (fractin) was quantified in the corpus callosum and in the ipsi- and contralateral cingulum. The percentage of area covered by Iba-1^{+} and GFAP[+]

Table 1
List of antibodies used for immunohistochemistry.

Antibody	Specificity	Company	Dilution
Rabbit Anti-Fractin	32 kDa Fractin fragment	Millipore (Etobicoke, ON, Canada)	1:500
Rabbit Anti-GFAP	Total GFAP protein	Cell Signaling (Beverly, MA, USA)	1:500
Rabbit Anti-Iba1	17 kDa calcium-binding protein	Wako (Osaka, Japan)	1:500
Alexa488-Goat Anti-rabbit IgG	Rabbit IgG (H + L) (secondary)	Life Technologies, Invitrogen	1:1000

immunolabelling was performed in the ipsilateral and contralateral sides of cortex, hippocampus and cingulum and in the corpus callosum. The values of the sections were averaged together to obtain one value per ROI for each animal.

2.4. Tissue preparation for biochemical and gene expression analysis

For protein and RNA preparation and gene expression analysis, 24 pups (n = 8 pups per group) were used. 24 h following the injection, the animals were deeply anaesthetized with isoflurane and transcardially perfused with saline. Brains were extracted, and the ipsilateral hemisphere was snap-frozen on dry ice. Ipsilateral brain hemispheres were reduced to powder by grinding the tissue in liquid nitrogen and the powder was kept at −80 °C until use.

2.4.1. Protein extraction and ELISA

For protein extraction, tissue powder was resuspended in RIPA buffer (100 mM Tris, pH 7.4, 150 mM NaCl, 1 mM EGTA, 1 mM EDTA, 1% Triton X-100, 0.5% sodium deoxycholate) with protease inhibitor cocktail and PMSF added. The suspension was incubated for 15 min and centrifuged at 10,000g for 15 min at 4 °C. Protein determination was performed using a standard Bradford protocol. Aliquots were made and kept frozen at −80 °C until use. In order to quantify the IL-1Ra in brain extracts of treated animals, an ELISA immunoassay was performed using a commercial rat IL-1Ra ELISA kit (TSZ Elisa, Biotang, Lexington, MA, USA).

2.4.2. RNA preparation and gene expression analysis

Total RNA was extracted with the RNeasy mini kit according to the manufacturer's instructions (Qiagen, Hilden, Germany). RNA quality and concentration were assessed by spectrophotometry using the Nanodrop apparatus (Thermoscientific, Wilmington, DE, USA). Total RNA (1 µg) was subjected to reverse transcription using the iScript™ cDNA synthesis kit (Bio-Rad, Hercules, CA, USA). RT-qPCR was performed in triplicate for each sample using SYBR Green Supermix (Bio-Rad. Hercules, CA, USA) for 40 cycles with a 3-step program (20 s of denaturation at 95 °C, 30 s of annealing at 58 °C and 30 s of extension at 72 °C). Amplification specificity was assessed with a melting curve analysis. The sequences of the primers used are provided in Table 2.

2.5. Statistics

All statistical analyses were performed using GraphPad Prism 7 software (GraphPad Software, La Jolla, CA). All data are presented as mean ± SEM. Comparisons between groups were performed using Kruskall-Wallis tests followed by Dunn's multiple comparisons test.

Statistical significance was set below 0.05.

3. Results

At P4, we did not see significant difference in body weight between the groups (Sham = 10.05 ± 0.20 g; LPS = 9.33 ± 0.30 g and LPS + IL-1Ra = 9.28 ± 0.12 g) but we noted a significant decrease in weight gain from P3 to P4 in the LPS (0.40 ± 0.18 g; p = 0.022) and LPS + IL-1Ra (0.45 ± 0.28 g; p = 0.043) animals compared to Sham (1.47 ± 0.22 g).

3.1. ^{1}H-MRS of the hippocampus.

24 h post-injection of lipopolysaccharide in the corpus callosum of rat pups, MRS was acquired in the ipsilateral hippocampus (Fig. 1A) on a 7 T scanner on 24 animals (8 Sham, 9 LPS, 7 LPS + IL-1Ra). The ipsilateral hippocampus was chosen to evaluate the detection of early signs of injury in a region known to undergo late atrophy (Lodygensky et al., 2005; Thompson et al., 2008; Thompson et al., 2014). Of the 24 spectra processed, 2 were rejected because one had insufficient resolution (linewidth > 20) and SNR, and another one had ROI placement errors, leaving a total of 22 spectra; 8 Sham, 8 LPS and 6 LPS + IL-1Ra. Glutamate, glutathione, N-acetylaspartate, phosphorylethanolamine and taurine were quantified in all spectra with a CRLB < 20%. GABA was also detected in all but one spectrum with a CRLB < 20%. Due to their resonance proximity in ^{1}H-MRS, creatine and phosphocreatine, glutamate and glutamine, N-acetylaspartate and N-acetylaspartylglutamate, and finally phosphocholine and glycerophosphocholine, were combined by two to allow better concentration estimation. For these combinations (respectively Cr + PCr, Glu + Gln, NAA + NAAG and PCh + GPC), concentrations could be estimated with a CRLB < 20% for all spectra except for PCh + GPC for which two spectra had a CRLB > 20%. Only GPC was not identified in more than 50% of the processed spectra.

3.1.1. Changes in metabolite and metabolite combination

From the metabolites and metabolite combination evaluated (Table 3), four had significant concentration changes between the Sham and LPS-treated groups (Fig. 1B). Glutamate (Glu), N-acetylaspartate (NAA), N-acetylaspartate + N-acetylaspartylglutamate (NAA + NAAG) and phosphorylethanolamine (PE) significantly decreased between Sham and LPS animals (Glu: p = 0.007; NAA: p = 0.01; NAA + NAAG: p = 0.001; PE: p = 0.02). For these metabolites, however, there was no significant difference between Sham and LPS + IL-1Ra group. We observed a general improvement of the four metabolites concentration changes induced by LPS in animals treated with IL-1Ra, particularly for

Table 2
List of primers used for gene expression analysis.

Gene	Forward (F) and Reverse (R) primer sequences	Ref.
GAPDH	**F-5′-AAGGTCGGTGTGAACGGATT-3′**	(Ma et al., 2015)
	R-5′-TGAACTTGCCGTGGGTAGAG-3′	
IL-1β	**F-5′-GGCAACTGTCCCTGAACTCAA-3′**	(Lodygensky et al., 2014)
	R-5′GCCTCAAAGAACAGGTCATTCTC-3′	
IL-6	**F-5′-TCCTACCCCAACTTCCAATGC-3′**	(Ma et al., 2015)
	R-5′TAGCACACTAGGTTTGCCGAG-3′	
iNOS	**F-5′-GAGTGAGGAGCAGGTTGAGGATTAC-3′**	(Chen et al., 2015)
	R-5′AGGAAAAGACCGCACCGAAG-3′	
MLKL	**F-5′-CCCGAGTTGTTGCAGGAGAT-3′**	(Liu et al., 2016)
	R-5′TCTCCAAGATTCCATCCGCAG-3′	
RIPK1	**F-5′-CTTAAGCCCAAGTGCAGTCA-3′**	(Zhao et al., 2016)
	R-5′ATAGCCCAACAAGGAGGATG-3′	
RIPK3	**F-5′-CAGTGTTGGCTGGAAGAGAA-3′**	(Zhao et al., 2016)
	R-5′AGGCTCAGAACTCCAGCAAT-3′	
TNF-α	**F-5′-CTATGTGCTCCTCACCCACA-3′**	(Rivera et al., 2013)
	R-5′TGGAAGACTCCTCCCAGGTA-3′	
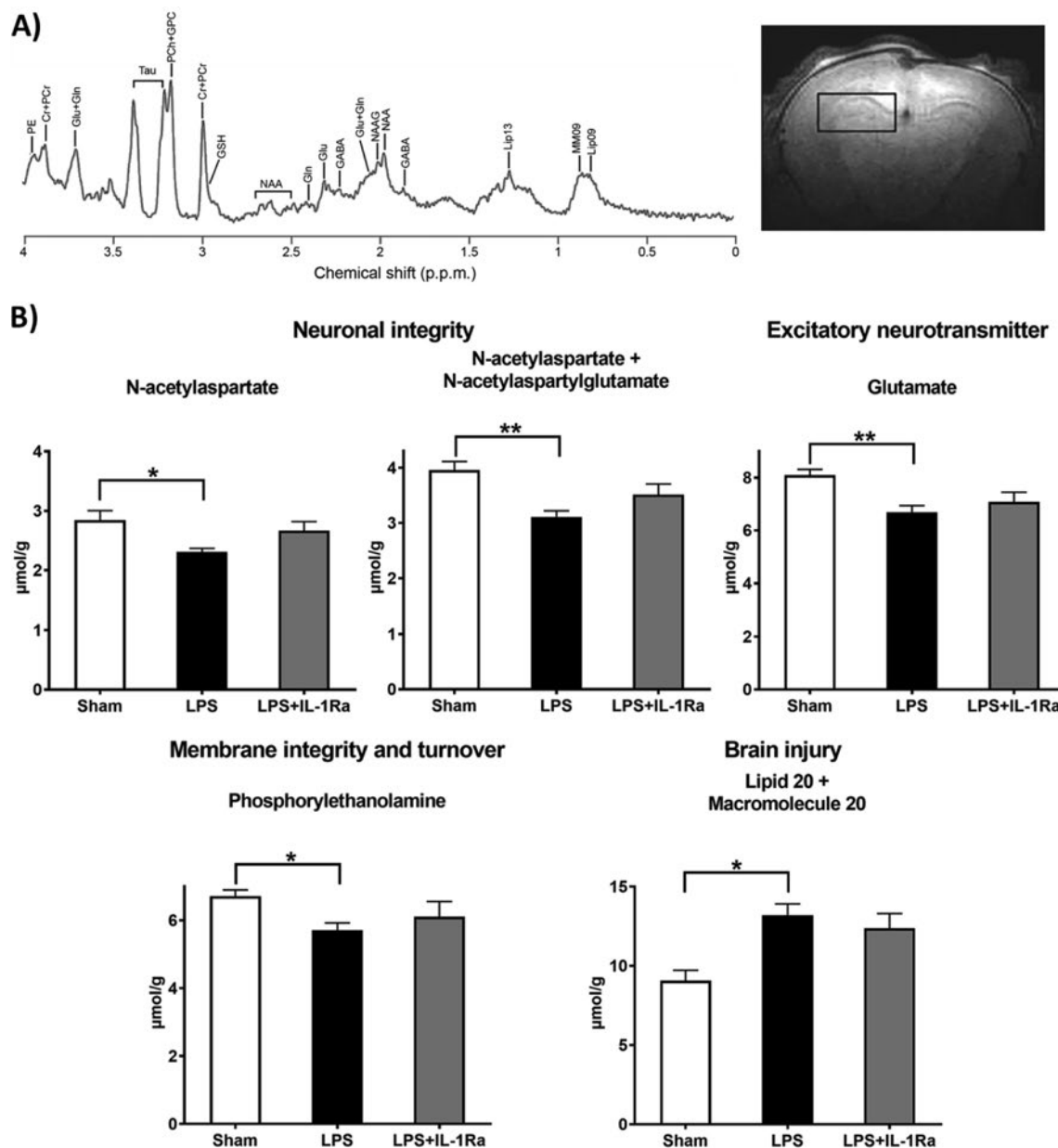
Fig. 1. Metabolites were evaluated by MRS 24 h following induction of inflammatory injury and IL1-Ra therapy. (A) Representative spectrum acquired on the ipsilateral hippocampus (highlighted in white rectangle on T2 weighted coronal image on P4 rats). (B) Bar graphs of metabolites concentration in the hippocampus; statistically significant changes compared to Sham are indicated. Values are represented as mean ± SEM. *p < 0.05; **p < 0.01; compared to Sham.

NAA and NAA + NAAG. NAA decreased of 19% for LPS (2.31 ± 0.06 μmol/g) and of 6% for LPS + IL-1Ra animals (2.67 ± 0.15 μmol/g); and NAA + NAAG (Fig. 1B) decreased of 21% in injured animals (3.11 ± 0.11 μmol/g) compared to 11% in treated animals (3.51 ± 0.19 μmol/g).

3.1.2. Changes in free lipids and Macromolecules

Lipid peaks are readily identifiable due to the ultrashort echo time used in the SPECIAL sequence. Of the 3 lipids and macromolecules concentrations measured (Table 3), a significant increase (p = 0.009) was found for the lipid 20 + macromolecule 20 (Lip20 + MM20), whose peak is highest at 2.0 ppm and were combined due to their resonance proximity. Lip20 + MM20 (Fig. 1B) concentration increased of 45% in the LPS group (13.19 ± 0.72 μmol/g) and of only 36% in the LPS + IL1-Ra group (12.38 ± 0.92 μmol/g) when compared to Sham animals (9.07 ± 0.65 μmol/g).

3.2. DTI study

DTI was acquired on 24 animals (Sham = 8, LPS = 9 and LPS + IL-1Ra = 7) to measure fractional anisotropy (FA), mean diffusivity (MD), axial diffusivity (AD) and radial diffusivity (RD) in the central part of the corpus callosum and in the ipsilateral and contralateral cingulum. Due to the presence of artifacts and/or blood, the ROIs could not be drawn in some animals of the LPS and LPS + IL-1Ra groups and, ROIs were drawn in all 8 Sham animals. Thus, in the corpus callosum, 8 LPS and 6 LPS + IL1-Ra were used; 6 LPS and 4 LPS + IL-1Ra were assessed for the ipsilateral cingulum and 7 LPS and 6 LPS + IL-1Ra for the contralateral cingulum.

We did not record any significant changes in FA values in the 3 regions evaluated (Fig. 2). Animals that received LPS had a significant decrease in MD and AD in the 3 ROIs evaluated (Fig. 2B, C and D) and RD decreased in the ipsilateral and contralateral cingulum (Fig. 2C and D). LPS + IL-1Ra group had significant decrease in RD in the corpus

Table 3
Concentrations of metabolites quantified in the ipsilateral hippocampus using the LCModel. Values are expressed as μmol/g (mean ± SEM). Concentrations in bold showed a statistical difference (*p < 0.05; **p < 0.01) compared to Sham animals (see Fig. 1).

Metabolites	Sham	LPS	LPS + IL-1Ra
Alanine	2.32 ± 0.25	2.43 ± 0.21	3.02 ± 0.61
Creatine + Phosphocreatine	6.65 ± 0.14	6.80 ± 0.28	6.63 ± 0.39
Creatine	5.38 ± 0.39	4.42 ± 0.73	4.34 ± 0.70
GABA	2.37 ± 0.14	2.04 ± 0.15	1.88 ± 0.18
Glutamine	2.47 ± 0.17	2.38 ± 0.17	2.53 ± 0.41
Glutamate	8.09 ± 0.22	**6.69 ± 0.25****	7.08 ± 0.37
Glutamate + Glutamine	10.29 ± 0.24	8.89 ± 0.43	9.35 ± 0.60
Glutathione	2.68 ± 0.16	2.22 ± 0.16	2.15 ± 0.14
Glycine	3.30 ± 0.15	2.86 ± 0.19	2.75 ± 0.18
N-acetylaspartate	2.84 ± 0.16	**2.31 ± 0.06***	2.67 ± 0.15
N-acetylaspartate + N-acetylaspartylglutamate	3.96 ± 0.16	**3.11 ± 0.11****	3.51 ± 0.19
Phosphocholine	1.44 ± 0.05	1.24 ± 0.11	1.34 ± 0.23
Phosphocholine + Glycerophosphocholine	1.53 ± 0.06	1.25 ± 0.09	1.47 ± 0.08
Phosphorylethanolamine	6.71 ± 0.18	**5.71 ± 0.21***	6.11 ± 0.45
Taurine	19.79 ± 0.57	19.31 ± 0.65	18.72 ± 0.78
Lipid 09 + macromolecule 09	14.27 ± 0.60	15.26 ± 0.88	16.15 ± 0.42
Lipid 20 + macromolecule 20	9.07 ± 0.65	**13.19 ± 0.72***	12.38 ± 0.92
Macromolecule 09	11.80 ± 1.06	10.20 ± 0.89	12.03 ± 0.55

callosum and contralateral cingulum. IL-1Ra treated animals had a significant restriction of MD in the corpus callosum and in the contralateral cingulum although to a lesser extent than LPS animals. There was no significative difference for AD values in the 3 ROIs between Sham and LPS + IL-1Ra group (Fig. 2E).

3.3. Immunohistological markers

To support the DTI/MRS results in the three groups evaluated in this study, immunohistological evaluations were performed to assess apoptosis (fractin), microgliosis (Iba-1) and astrogliosis (GFAP.
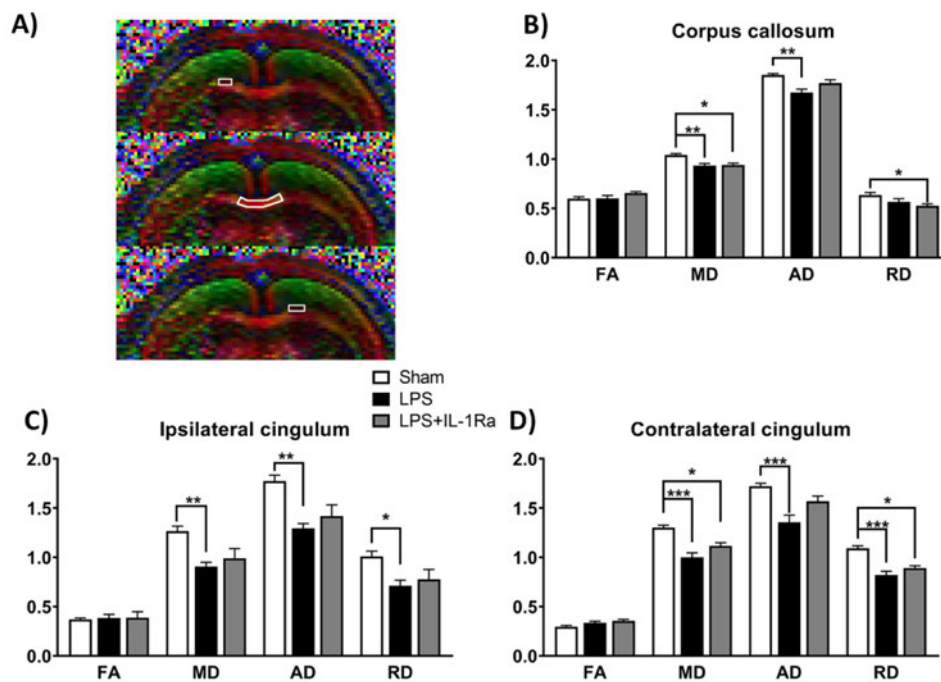
Fig. 2. *In vivo* diffusion tensor imaging of P4 rat pups acquired in each group. (A) Example of coronal RGB (red, green, and blue) map with the ROIs (ipsilateral cingulum, corpus callosum and contralateral cingulum) highlighted in white. The colors in the RGB map represent the preferred direction of water diffusion. Red corresponds to medial-lateral, green to superior–inferior, and blue to rostral–caudal directions. (B, C and D) Bar graph of fractional anisotropy (FA), mean diffusivity (MD), axial diffusivity (AD) and radial diffusivity (RD) in the (B) corpus callosum, (C) ipsilateral cingulum and (D) contralateral cingulum. (E) Table of scalar map values represented as mean ± SEM. *: P < 0.05; **: P < 0.01; ***: P < 0.001 compared to the Sham. Diffusivity: μm²/ms. (For interpretation of the references to colour in this figure legend, the reader is referred to the web version of this article.)

	Corpus Callosum			Ipsilateral Cingulum			Controlateral Cingulum		
	Sham (n=8)	LPS (n=8)	LPS+ IL1Ra (n=6)	Sham (n=8)	LPS (n=6)	LPS+ Il-1Ra (n=4)	Sham (n=8)	LPS (n=7)	LPS+ Il-1Ra (n=6)
FA	0.60 ± 0.02	0.60 ± 0.03	0.66 ± 0.02	0.36 ± 0.02	0.38 ± 0.04	0.39 ± 0.06	0.30 ± 0.01	0.33 ± 0.02	0.35 ± 0.02
MD	1.01 ± 0.02	**0.93 ± 0.02****	**0.94 ± 0.02***	1.27 ± 0.05	**0.91 ± 0.04****	0.99 ± 0.10	1.30 ± 0.02	**1.00 ± 0.05*****	**1.12 ± 0.03***
AD	1.85 ± 0.01	**1.67 ± 0.03****	1.77 ± 0.03	1.78 ± 0.06	**1.29 ± 0.05****	1.42 ± 0.12	1.72 ± 0.03	**1.36 ± 0.07*****	1.57 ± 0.05
RD	0.63 ± 0.03	0.57 ± 0.03	**0.53 ± 0.02***	1.01 ± 0.05	**0.71 ± 0.05***	0.78 ± 0.10	1.09 ± 0.03	**0.82 ± 0.04*****	**0.89 ± 0.02***
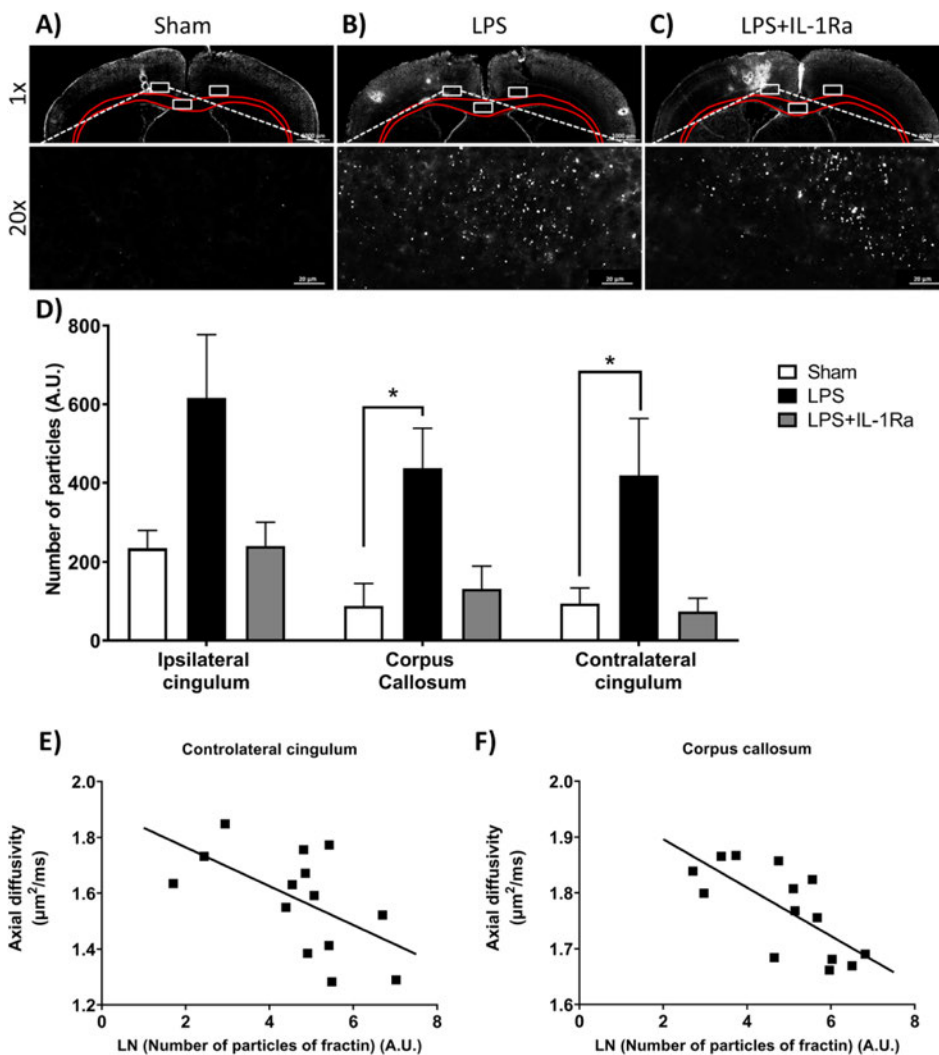
Fig. 3. Post-mortem evaluation of the apoptotic marker fractin. (A-C) Representative images for each group: (A) Sham, (B) LPS (C) LPS + IL-1Ra. (D) Bar graph of the number of fractin$^+$ particles expression in the corpus callosum, ipsilateral and contralateral cingulum. In the images at $1\times$, the boxed areas represent the regions of interest obtained at $20\times$, images correspond to the ipsilateral cingulum. Scatter plot of the axial diffusivity for the natural logarithm of the fractin quantification in (E) the contralateral cingulum, with the following regression line: AD $= -0.070 \times$ ln(fractin) + 1.90; $R^2 = 0.33$, P = 0.03 and (F) the corpus callosum, with the following regression line: AD $= -0.043 \times$ ln (fractin) + 1.98; $R^2 = 0.52$, P = 0.003. Values are represented as mean ± SEM. Bars: $1\times = 1000\,\mu m$, $20\times = 20\,\mu m$. *p < 0.05, compared to Sham.

3.3.1. Apoptosis

The marker of apoptosis fractin was expressed in the ROIs evaluated in the three groups (Fig. 3A–C). Compared to Sham animal, LPS exposed animals had increased fractin expression in the 3 ROIs and the difference were significant in the corpus callosum and contralateral cingulum (Fig. 3D). A slight reaction was observed in the ipsilateral cingulum of the Sham animal near the site of the injection (Fig. 3A) that could contribute to the increased value in this region compared to the other two (Fig. 3D). The LPS + IL-1Ra group had markedly improved fractin expression compared to LPS group, though the values were not significant. Knowing that we have previously shown that diffusion restriction had an inverse correlation with cell death marker expression, we looked at possible interactions between fractin expression and DTI. We found that fractin expression had a negative correlation to AD in the corpus callosum and contralateral cingulum and this correlation was stronger in the corpus callosum compared to the contralateral cingulum (Fig. 3E and F).

3.3.2. Microgliosis

Microgliosis was assessed by immunolabelling brain slices with Iba-1 (Fig. 4). LPS exposure induced bilateral microglia activation within the different ROIs as seen with increased Iba-1 expression (Fig. 4A and B). Compared to the sham group, Iba-1 expression increased significantly in the ipsilateral and contralateral cortex of LPS animals (Fig. 4B). Treatment with IL-1Ra induced a slight decrease in Iba-1 expression particularly in the hippocampus (Fig. 4B). Correlation

analyses were performed between Iba-1 expression and changes seen in the DTI and MRS in corresponding ROIs. From the metabolites we measured by MRS, we looked at correlation between Iba-1expression and metabolites associated to microglia activation and neuroinflammation which includes total creatine, total choline, glutamate and the free lipids and macromolecules (Zahr et al., 2014; Pardon et al., 2016). We did not observe any significant correlation between Iba-1 expression and the metabolites of interest, although we observed trends between creatine (r = -0.62, p = 0.06) and Lip20 + MM20 (r = 0.46, p = 0.08) and Iba-1 expression. Correlation analysis with the different DTI parameters showed that Iba-1 expression was inversely associated to AD in the corpus callosum and contralateral cingulum (Fig. 4C and D) and also, to MD in the contralateral cingulum (Fig. 4D).

3.3.3. Astrogliosis

Astrocyte activation was quantified on brain slices marked with GFAP (Fig. 5). Images in Fig. 5 showed that, LPS exposure induced an important astroglial reaction, which was partially dimmed by a treatment with IL-1Ra (Fig. 5A). Quantification of GFAP immunolabelling demonstrated that LPS induced a significant increase in astrocyte activation in the contralateral cingulum and the treatment with IL-1Ra tended to decrease it (p = 0.085) (Fig. 5B). Quantification of astrogliosis revealed a strong reaction in the cortex of LPS exposed animals compared to Sham although it did not reach statistical significance (Fig. 5B). However, LPS did not seem to influence astrocyte activation in the ipsi- and contralateral hippocampus and in the corpus callosum
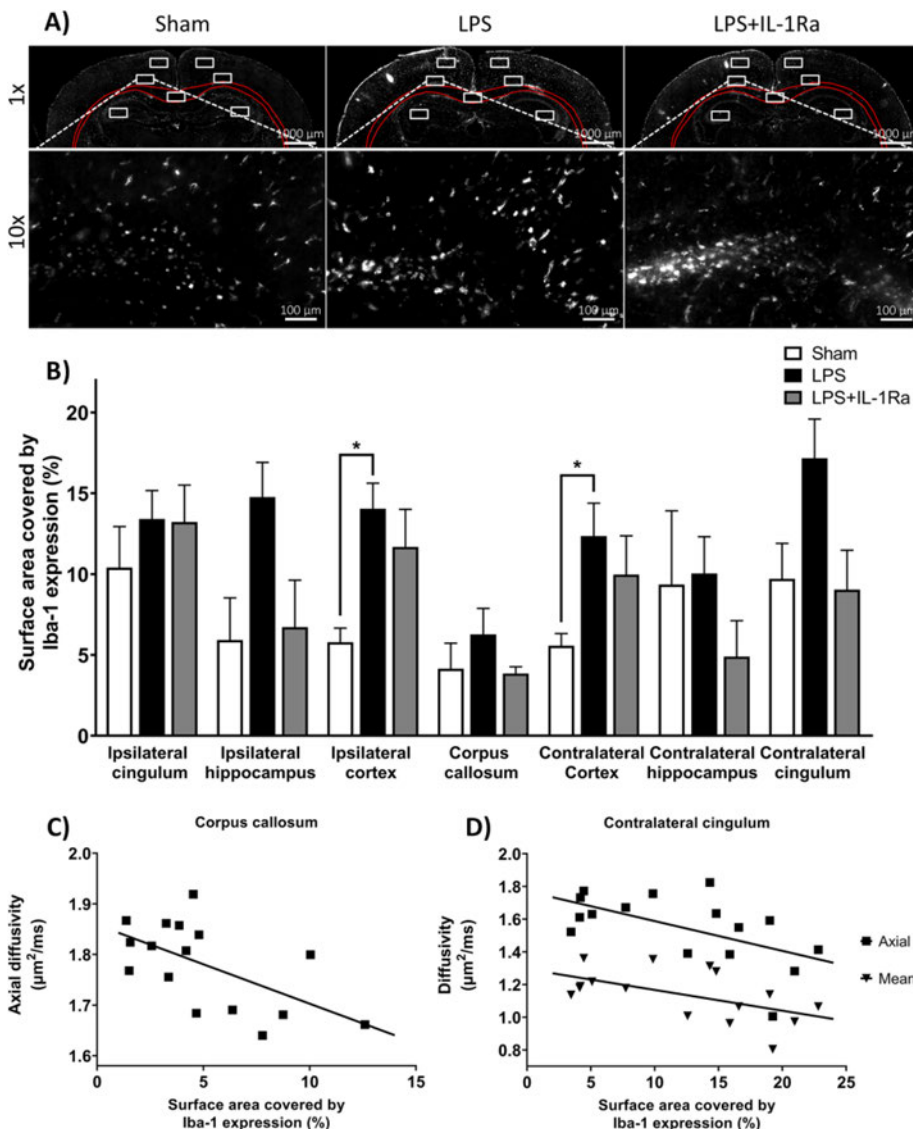
Fig. 4. Evaluation of microglia activation by Iba-1 immunohistochemistry. (A) Representative images for Sham, LPS and LPS + IL-1Ra animals taken at 1× and 10× using Zeiss AxioScan. (B) Bar graph of the percentage of the area covered by Iba-1 expression in the ROIs. The corpus callosum is highlighted in red. In the images at 1×, the boxed areas represent ROIs; images at 10× correspond to the ipsilateral cingulum. (C) Scatter plot of the AD effect for Iba-1 expression in the corpus callosum, with the following regression line: AD = −0.016 × Iba-1 expression + 1.86; R^2 = 0.35, P = 0.015 (D) Scatter plot of the AD and MD effects for Iba-1 expression in the contralateral cingulum, with the following regression lines: AD = −0.018 × Iba-1 expression + 1.77; R^2 = 0.33, P = 0.02 and MD = −0.013 × Iba-1 expression + 1.29; R^2 = 0.30, P = 0.027. Bars: 1× = 1000 μm, 10× = 100 μm. *p < 0.05.

(Fig. 5B). Correlation analysis between immunohistochemistry and MRS/DTI were done. For MRS, we evaluated the correlation between GFAP in the ipsilateral hippocampus and the following metabolites myo-inositol, GSH, glutamine, glutamate, and lactate that are associated to astrogliosis (Xu et al., 2011; Harris et al., 2015). Unfortunately, we were not able to quantify myo-Inositol and lactate with sufficient precision in our study. We did not observe any significant correlation between the 3 remaining metabolites and GFAP expression in the ipsilateral hippocampus, but we saw a trend toward an interaction between GFAP expression and glutamine (r = 0.54, p = 0.09). Assessment of correlation between DTI and GFAP expression revealed an inverse relationship between radial diffusivity and the extent of astrocytic activation in the ipsilateral and contralateral cingulum (Fig. 5C and D).

3.4. Intracerebral level of IL-1Ra:

To confirm the presence of IL-1Ra within the brain parenchyma following its systemic injection, we performed an ELISA with extracts from the ipsilateral brain hemisphere. LPS + IL-1Ra had a significant increase in cerebral IL-1Ra concentration compared to the Sham and LPS groups (p < 0.05, Fig. 6). This result suggests that the 23% increase in IL-1Ra is due to the presence of the recombinant IL-1Ra in the ipsilateral brain hemisphere.

3.5. RNA expression:

The expressions of mRNA for pro-inflammatory (IL-1β, IL-6, iNOS and TNF-α) and necroptotic (RIPK1, RIPK3 and MLKL) genes in the ipsilateral brain hemisphere were determined by quantitative PCR (qPCR). Compared to the sham group, the LPS had a strong inflammatory response for the 4 pro-inflammatory genes tested (Fig. 7). IL-1ra treatment decreased LPS-induced expression of pro-inflammatory genes particularly for IL-1β and iNOS (Fig. 7).

Compared to Sham animals, LPS animals had a significant increase in the expression of the 3 genes related to necroptosis (Fig. 8). Animals treated with IL-1Ra had a significant increased expression of RIPK3 and MLKL but not of RIPK1 (Fig. 8). IL-1Ra treatment decreased the LPS-induced expression of RIPK3 and MLKL respectively by 27.53% and 15.83% (Fig. 8).

4. Discussion

The present study provides new insights on the use of multimodal MRI as an early monitoring tool of inflammatory injury and therapeutic response in the immature rat brain.
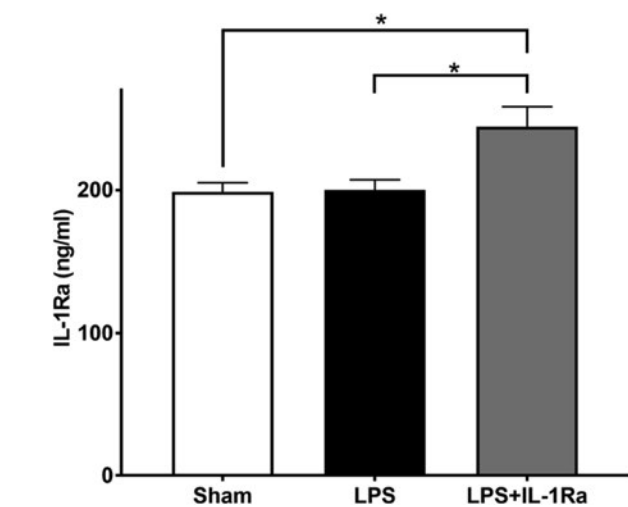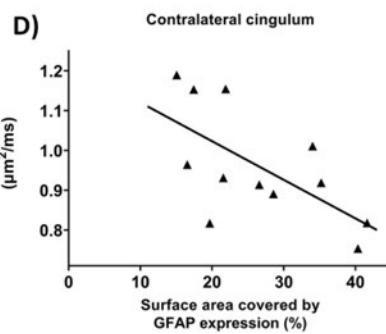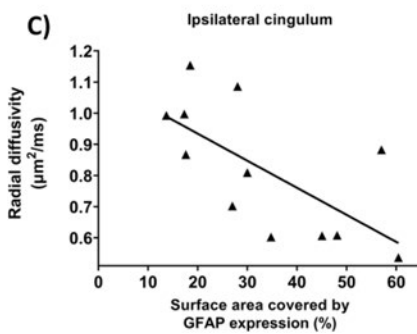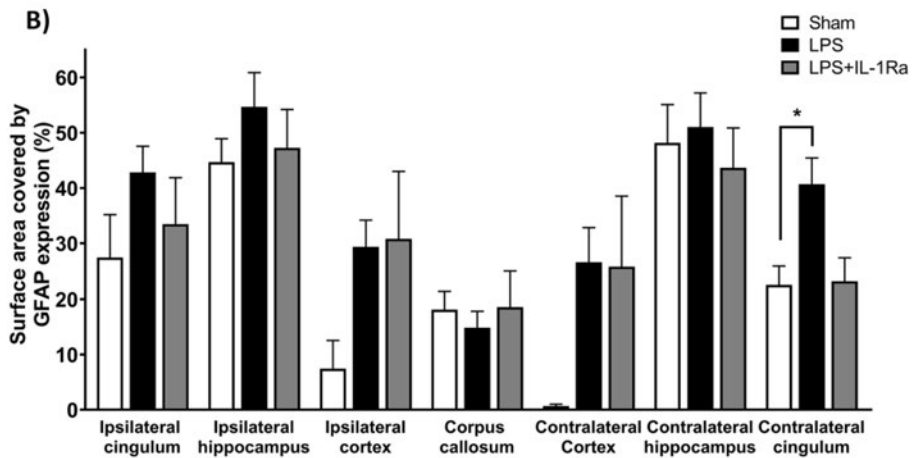
Fig. 5. Evaluation of astrocyte activation by immunohistochemistry with GFAP. (A) Representative images for Sham, LPS and LPS + IL-1Ra animals taken at $1\times$ and $10\times$ using Zeiss AxioScan. (B) Bar graph of the surface covered by GFAP expression in the different regions of interest. In the images at $1\times$, the boxed areas represent the regions of interest; at $10\times$, images correspond to the ipsilateral cortex. (C-D) Scatter plot of the RD effect for GFAP expression in (C) the ipsilateral cingulum, with the following regression line: RD $= -0.009 \times$ GFAP expression + 1.11; $R^2 = 0.45$, P = 0.018 and (D) the contralateral cingulum, with the following regression lines: RD $= -0.010 \times$ GFAP expression + 1.22; $R^2 = 0.41$, P = 0.026. Bars: $1\times = 1000\,\mu m$, $10\times = 100\,\mu m$. *p < 0.05.
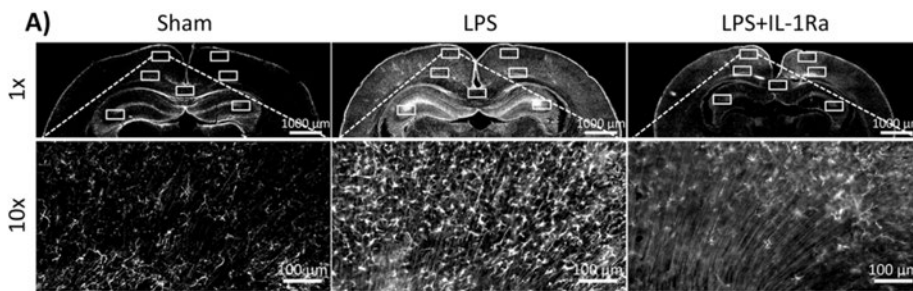

Fig. 6. IL-1Ra concentration measured by ELISA in the ipsilateral brain hemisphere. Results are presented in ng/ml (mean ± SEM). *p < 0.05.

4.1. Neonatal LPS exposure alters the hippocampal metabolism

Using ^{1}H-MRS, we showed that intracerebral LPS induced acute metabolic changes in the hippocampus, which precede the late atrophy known to occur in this preclinical model (Wang et al., 2013). In accordance to previously published results, we observed a decrease in the NAA and NAA + NAAG levels in injured animals typically known to be associated with impaired neuronal integrity (Lodygensky et al., 2014; van de Looij et al., 2014a; van de Looij et al., 2014b). In our study, glutamate levels in the hippocampus decreased following LPS exposure in a similar manner to changes seen during the acute phase of neonatal hypoxia-ischemia (van de Looij et al., 2011; Sanches et al., 2018) and in the striatum of adult rats subjected to quinolinic acid injury (Tkac et al., 2001). The decrease in glutamate level can reflect altered neurotransmitter production following neuronal cell death and, it could also represent changes in the glutamate-glutamine cycle between neurons and glia. We also measured decreased levels of phosphorylethanolamine (PE), a precursor of phosphatidylethanolamine, and, a decrease in PE levels was associated to myelination impairments and also to sign of lower cellular proliferation in perinatal hypoxia-ischemia (Raman et al., 2005; Wang et al., 2016). Moreover, PE levels reduction could reflect a weakened antioxidative status in the brain since PE is a substrate in sphingolipid peroxidation (Han et al., 2017). The concentration of lipid 20 and macromolecule 20 increased following LPS

Genetic expression of pro-inflammatory markers
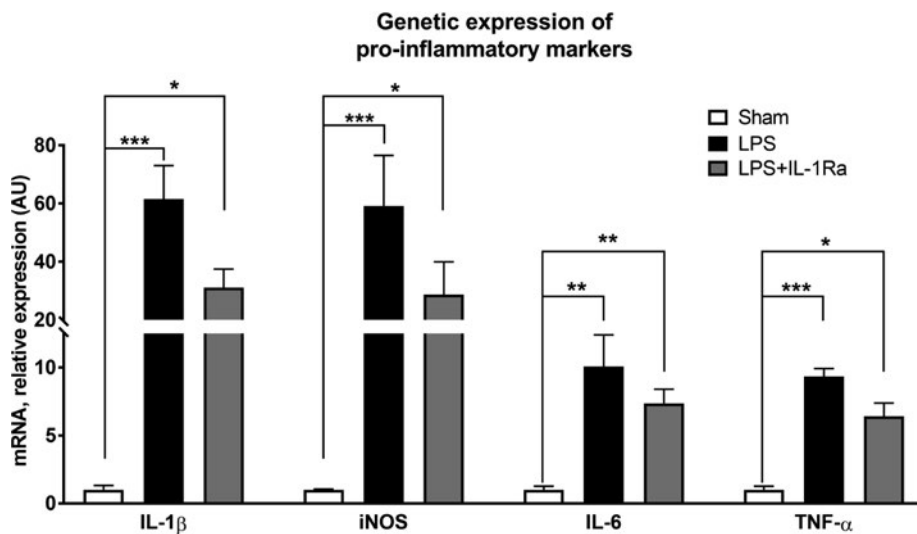
Fig. 7. Changes in pro-inflammatory gene expression in brain of P4 rat pups. Relative mRNA levels are presented in arbitrary units (AU, mean ± SEM) compared to Sham group. n = 8 per group. IL-1β, interleukin 1β; IL-6, interleukin 6; iNOS, inducible nitric oxide synthase, and TNF-α, tumor necrosis factor α. $^*p < 0.05$; $^{**}p < 0.01$; $^{***}p < 0.001$ compared to Sham.

injury similarly to data published on this model (Lodygensky et al., 2014). Increase in lipids and macromolecules was seen as a sign of microglial cell activation in adult mice subjected to systemic LPS (Pardon et al., 2016) and also in tumors (Yamasaki et al., 2015). In brain tumors, increase in lipid and macromolecule concentrations was associated with membrane rupture and cell death (Sijens et al., 1996; Nakamura et al., 2018).

4.2. DTI

DTI is a sensitive tool that allows *in vivo* evaluation of cerebral microstructure and is very sensitive to changes following injury. Although the exact mechanisms and cell types associated to the different diffusivity parameters have not been accurately identified yet, studies suggest that axial and radial diffusivity could reflect the integrity of axonal and myelin content (Zhang et al., 2012; Tuor et al., 2014; Stolp et al., 2018). However the theory is more complex in the setting of a young and immature brain and acute injury. In accordance to published results for both preterm infants and animal models with WMI, we recorded, during the acute phase of injury, a decrease in diffusivity (AD, RD and MD) following LPS exposure without changes in fractional anisotropy (Lodygensky et al., 2011; Lodygensky et al., 2014; Tuor et al., 2014). Moreover, changes in axial diffusivity correlated to fractin expression in the corpus callosum and contralateral cingulum

and also, to a lesser extent, with microgliosis. Radial diffusivity had an inverse correlation with astrogliosis in the ipsilateral and contralateral cingulum. The changes in axial diffusivity are probably a reflection of combined ongoing damage with increase in cell death, microglial activation and axonal beading (Budde and Frank, 2010; Xie et al., 2010). The changes in radial diffusivity seen in this study, at an age prior to the onset of myelination, could represent ongoing astrogliosis and could also be related to axonal injury as it was seen in animal model of neonatal stroke and in traumatic brain injury (Zhuo et al., 2012; Tuor et al., 2014; Singh et al., 2016). Thus, DTI parameters alteration could be a reflection of the acute neuroinflammatory response characterized by astrocyte activation, microgliosis and apoptotic cell death.

4.3. Neonatal LPS exposure leads to inflammation and cell death

LPS activation of toll like receptor 4 (TLR-4) induces a pro-inflammatory phenotype characterized by microglia activation, astrogliosis, inflammatory marker expression and cell death via both caspase-dependant (apoptosis) and caspase-independent (necroptosis) pathways (Nikseresht et al., 2015; Savard et al., 2015). Similarly to previous results in this animal model at P3 and P5, LPS exposure at P3 induced a strong neuroinflammatory profile with the expression of the pro-inflammatory markers IL-1β, iNOS, IL-6 and TNF-α, gliosis (increase Iba-1 and GFAP expression) and expression of both apoptotic and

Genetic expression of necroptosis regulatory protein
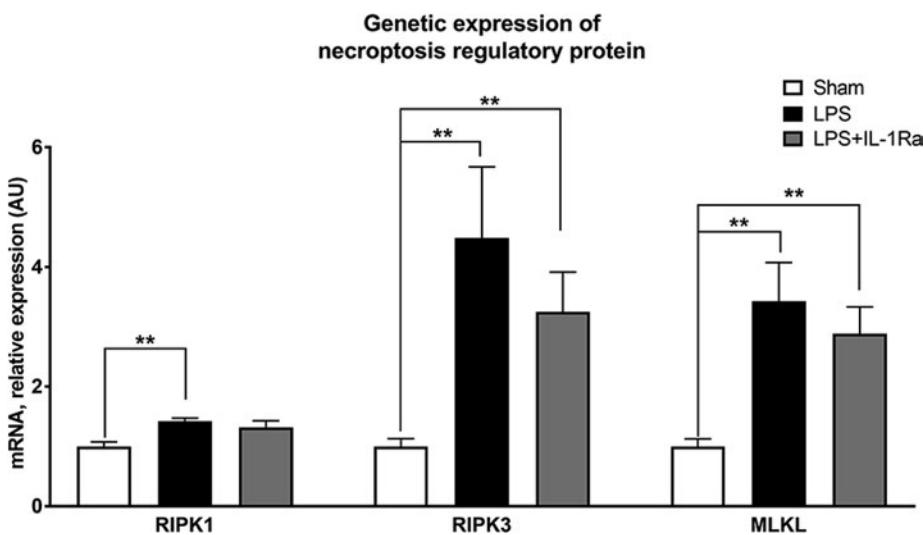
Fig. 8. Changes in necroptotic gene expression in brain of P4 rat pups 24 h after exposure. Relative mRNA levels are presented in arbitrary units (AU, mean ± SEM) compared to Sham group. n = 8 per group. RIPK1, Receptor-interacting serine/threonine-protein kinase 1; RIPK3, Receptor-interacting serine/threonine-protein kinase 3; MLKL, Mixed Lineage Kinase Domain-Like protein. $^{**}p < 0.01$ compared to Sham.

necroptosis markers (Pang et al., 2003; Lodygensky et al., 2014). To our knowledge, it is the first time that the LPS-induced expression of necroptosis markers is shown in the intracerebral LPS-injection model. It was previously demonstrated that, following neonatal hypoxia, necroptosis was associated to neuronal and oligodendrocytes cell death and disruption of normal myelination process (Qu et al., 2016; Qu et al., 2017). Furthermore, RIPK3 and MLKL expression can increase the activity of the NLRP3 inflammasome which favors the establishment of a pro-inflammatory state via IL-1β production (Lawlor et al., 2015).

4.4. Early indication of IL-1Ra neuroprotective effect during the acute injury phase

During the acute phase of injury, although the effect of IL-1Ra did not reach statistical significance levels, we observed that IL-1Ra exerted partial neuroprotective effect with similar trends in *in vivo* MRI and immunohistochemistry and gene expression analysis. The effect of therapy at this point cannot be expected to be complete as the animals were only exposed to 3 injections. In Girard et al. study, IL-1Ra showed neuroprotective trends during the acute phase of injury (24–48 h post-injury) in an animal model of adult stroke, but its neuroprotective and restorative effects were more prominent when assessed at later time points (Girard et al., 2014). If animals would have been imaged and analyzed at later time points, DTI and MRS biomarkers of acute injury would not have been usable and the cytokine storm would be over. Indeed, the mean diffusivity reduction is only present in the first days following LPS (Lodygensky et al., 2010; Lodygensky et al., 2014). Furthermore, *in vivo* MRI is highly relevant when performed during an acute event as it can determine the immediate effect of therapy so that it could be replaced if found inefficient, similarly to its use in glioblastoma multiform management (Rygh et al., 2014; de Souza et al., 2015; Toussaint et al., 2017). We demonstrate here for the first time that the first stages of a neuroprotective effect could be identified using *in vivo* DTI and MRS, which gives complementary information during the acute inflammatory injury. These changes were similar to cell death and inflammatory markers evaluated by immunohistochemical and biochemical methods. In human preterm infants, early imaging was shown to be superior in detecting WMI and predicting outcomes (Inder et al., 1999; Martinez-Biarge et al., 2016; Guo et al., 2017; Nguyen et al., 2019). With the development of new MRI systems for the Neonatal Intensive Care Unit (Tkach et al., 2013; Merhar et al., 2017), sequential imaging will be easier to perform and assist in the early injury detection and monitoring of therapy.

4.5. Limitations

One limit of this study is the initiation of IL-1Ra therapy within 5 min of inflammation onset. The timing of therapy was based on the kinetics as aforementioned. By starting therapy early, we maximised the chances to detect positive changes. We believe that the translational value is still present as the available timeframe is wider in human preterm infants. Another limitation is the fact that, although DTI is more sensitive than conventional MRI in early detection of brain injury, it lacks specificity in regard to the physiological processes involved (Winklewski et al., 2018; Novikov et al., 2019). Therefore, the development of new techniques and models to analysis diffusion that goes beyond the use of tensors would lead to a better understanding of the contribution of different pathophysiological mechanisms on diffusivity changes during the acute and chronic phase of injury. Nonetheless, the presence of correlation between DTI and immunohistochemical markers underlines its potential to detect the early neuroinflammatory reaction and therapeutic response in neonatal WMI.

5. Conclusion

In conclusion, we showed that *in vivo* DTI reflected ongoing neuroinflammation as seen with histology, and MRS detected early metabolic changes in the hippocampus prior to appearance of histological signs of injury. Furthermore, DTI and MRS showed early signs of response to neuroprotection during the acute phase of injury. If confirmed in other animal models, these results would suggest that *in vivo* multimodal MRI can detect not only the first stage of major white matter injury and metabolic impairment but assess the effect of therapy. As clinical MRI is being used more and more in the neonatal intensive care unit, it is highly relevant to evaluate the potential role of MRI as a central part in the design of future neuroprotective trials in human neonates.

Author Contributions

Wyston Pierre participated in data acquisition, data analysis, and manuscript draft, reviewed and revised the manuscript. Luis Akakpo contributed to data acquisition, data analysis and manuscript preparation. Irène Londono and Philippe Pouliot contributed to the study preparation, data acquisition and manuscript preparation. Sylvain Chemtob and Frédéric Lesage has participated in the conceptualization of the study and revised the manuscript. Gregory Anton Lodygensky conceptualized and designed the study, contributed to data acquisition, supervised the data analysis, and revised the manuscript.

Declaration of Competing Interest

The authors declare no competing financial interests.

Acknowledgement

References

Back, S.A., Rosenberg, P.A., 2014. Pathophysiology of glia in perinatal white matter injury. Glia.

Bathen, T.F., Heldahl, M.G., Sitter, B., Vettukattil, R., Bofin, A., Lundgren, S., Gribbestad, I.S., 2011. In vivo MRS of locally advanced breast cancer: characteristics related to negative or positive choline detection and early monitoring of treatment response. Magma 24, 347–357.

Budde, M.D., Frank, J.A., 2010. Neurite beading is sufficient to decrease the apparent diffusion coefficient after ischemic stroke. Proc. Natl. Acad. Sci. USA 107, 14472–14477.

Cai, Z., Lin, S., Pang, Y., Rhodes, P.G., 2004. Brain injury induced by intracerebral injection of interleukin-1beta and tumor necrosis factor-alpha in the neonatal rat. Pediatr. Res. 56, 377–384.

Cai, Z., Pang, Y., Lin, S., Rhodes, P.G., 2003. Differential roles of tumor necrosis factor-alpha and interleukin-1 beta in lipopolysaccharide-induced brain injury in the neonatal rat. Brain Res. 975, 37–47.

Cao, M.D., Sitter, B., Bathen, T.F., Bofin, A., Lonning, P.E., Lundgren, S., Gribbestad, I.S., 2012. Predicting long-term survival and treatment response in breast cancer patients receiving neoadjuvant chemotherapy by MR metabolic profiling. NMR Biomed. 25, 369–378.

Caverzasi, E., Pichiecchio, A., Poloni, G.U., Calligaro, A., Pasin, M., Palesi, F., Castellazzi, G., Pasquini, M., Biondi, M., Barale, F., Bastianello, S., 2012. Magnetic resonance spectroscopy in the evaluation of treatment efficacy in unipolar major depressive disorder: a review of the literature. Funct. Neurol. 27, 13–22.

Chen, S.H., Oyarzabal, E.A., Sung, Y.F., Chu, C.H., Wang, Q., Chen, S.L., Lu, R.B., Hong, J.S., 2015. Microglial regulation of immunological and neuroprotective functions of astroglia. Glia 63, 118–131.

de Souza, P.C., Balasubramanian, K., Njoku, C., Smith, N., Gillespie, D.L., Schwager, A., Abdullah, O., Ritchey, J.W., Fung, K.M., Saunders, D., Jensen, R.L., Towner, R.A., 2015. OKN-007 decreases tumor necrosis and tumor cell proliferation and increases apoptosis in a preclinical F98 rat glioma model. J. Magn. Reson. Imaging 42, 1582–1591.

Dinarello, C.A., Simon, A., van der Meer, J.W.M., 2012. Treating inflammation by blocking interleukin-1 in a broad spectrum of diseases. Nat. Rev. Drug Discovery 11,

633–652.

Fan, L.W., Mitchell, H.J., Rhodes, P.G., Cai, Z., 2008a. Alpha-Phenyl-n-tert-butyl-nitrone attenuates lipopolysaccharide-induced neuronal injury in the neonatal rat brain. Neuroscience 151, 737–744.

Fan, L.W., Pang, Y., Lin, S., Tien, L.T., Ma, T., Rhodes, P.G., Cai, Z., 2005. Minocycline reduces lipopolysaccharide-induced neurological dysfunction and brain injury in the neonatal rat. J. Neurosci. Res. 82, 71–82.

Fan, L.W., Tien, L.T., Mitchell, H.J., Rhodes, P.G., Cai, Z., 2008b. Alpha-phenyl-n-tert-butyl-nitrone ameliorates hippocampal injury and improves learning and memory in juvenile rats following neonatal exposure to lipopolysaccharide. Eur. J. Neurosci. 27, 1475–1484.

Fan, L.W., Tien, L.T., Zheng, B., Pang, Y., Lin, R.C., Simpson, K.L., Ma, T., Rhodes, P.G., Cai, Z., 2011. Dopaminergic neuronal injury in the adult rat brain following neonatal exposure to lipopolysaccharide and the silent neurotoxicity. Brain Behav. Immun. 25, 286–297.

Favrais, G., van de Looij, Y., Fleiss, B., Ramanantsoa, N., Bonnin, P., Stoltenburg-Didinger, G., Lacaud, A., Saliba, E., Dammann, O., Gallego, J., Sizonenko, S., Hagberg, H., Lelievre, V., Gressens, P., 2011. Systemic inflammation disrupts the developmental program of white matter. Ann. Neurol. 70, 550–565.

Galinsky, R., Lear, C.A., Dean, J.M., Wassink, G., Dhillon, S.K., Fraser, M., Davidson, J.O., Bennet, L., Gunn, A.J., 2018. Complex interactions between hypoxia-ischemia and inflammation in preterm brain injury. Dev. Med. Child Neurol. 60, 126–133.

Girard, S., Murray, K.N., Rothwell, N.J., Metz, G.A.S., Allan, S.M., 2014. Long-term functional recovery and compensation after cerebral ischemia in rats. Behav. Brain Res. 270, 18–28.

Girard, S., Sebire, G., Kadhim, H., 2010. Proinflammatory orientation of the interleukin 1 system and downstream induction of matrix metalloproteinase 9 in the pathophysiology of human perinatal white matter damage. J. Neuropathol. Exp. Neurol. 69, 1116–1129.

Girard, S., Sebire, H., Brochu, M.E., Briota, S., Sarret, P., Sebire, G., 2012. Postnatal administration of IL-1Ra exerts neuroprotective effects following perinatal inflammation and/or hypoxic-ischemic injuries. Brain Behav. Immun. 26, 1331–1339.

Gruetter, R., 1993. Automatic, localized in vivo adjustment of all first- and second-order shim coils. Magn. Reson. Med. 29, 804–811.

Guo, T., Duerden, E.G., Adams, E., Chau, V., Branson, H.M., Chakravarty, M.M., Poskitt, K.J., Synnes, A., Grunau, R.E., Miller, S.P., 2017. Quantitative assessment of white matter injury in preterm neonates: Association with outcomes. Neurology 88, 614–622.

Han, B., Wang, J.H., Geng, Y., Shen, L., Wang, H.L., Wang, Y.Y., Wang, M.W., 2017. Chronic stress contributes to cognitive dysfunction and hippocampal metabolic abnormalities in APP/PS1 mice. Cell. Physiol. Biochem. 41, 1766–1776.

Harris, J.L., Choi, I.Y., Brooks, W.M., 2015. Probing astrocyte metabolism in vivo: proton magnetic resonance spectroscopy in the injured and aging brain. Front. Aging Neurosci. 7, 202.

Inder, T., Huppi, P.S., Zientara, G.P., Maier, S.E., Jolesz, F.A., di Salvo, D., Robertson, R., Barnes, P.D., Volpe, J.J., 1999. Early detection of periventricular leukomalacia by diffusion-weighted magnetic resonance imaging techniques. J. Pediatr. 134, 631–634.

Inder, T.E., Anderson, N.J., Spencer, C., Wells, S., Volpe, J.J., 2003. White matter injury in the premature infant: a comparison between serial cranial sonographic and MR findings at term. AJNR Am. J. Neuroradiol. 24, 805–809.

Jin, C., Londono, I., Mallard, C., Lodygensky, G.A., 2015. New means to assess neonatal inflammatory brain injury. J. Neuroinflammation 12, 180.

Khwaja, O., Volpe, J.J., 2008. Pathogenesis of cerebral white matter injury of prematurity. Arch. Dis. Child. Fetal Neonatal. Ed. 93, F153–161.

Lawlor, K.E., Khan, N., Mildenhall, A., Gerlic, M., Croker, B.A., D'Cruz, A.A., Hall, C., Kaur Spall, S., Anderton, H., Masters, S.L., Rashidi, M., Wicks, I.P., Alexander, W.S., Mitsuuchi, Y., Benetatos, C.A., Condon, S.M., Wong, W.W., Silke, J., Vaux, D.L., Vince, J.E., 2015. RIPK3 promotes cell death and NLRP3 inflammasome activation in the absence of MLKL. Nat. Commun. 6, 6282.

Lee, S.C., Liu, W., Dickson, D.W., Brosnan, C.F., Berman, J.W., 1993. Cytokine production by human fetal microglia and astrocytes. Differential induction by lipopolysaccharide and IL-1 beta. J. Immunol. 150, 2659.

Liu, T., Zhao, D.X., Cui, H., Chen, L., Bao, Y.H., Wang, Y., Jiang, J.Y., 2016. Therapeutic hypothermia attenuates tissue damage and cytokine expression after traumatic brain injury by inhibiting necroptosis in the rat. Sci. Rep. 6, 24547.

Lodygensky, G.A., Kunz, N., Perroud, E., Somm, E., Mlynarik, V., Huppi, P.S., Gruetter, R., Sizonenko, S.V., 2014. Definition and quantification of acute inflammatory white matter injury in the immature brain by MRI/MRS at high magnetic field. Pediatr. Res. 75, 415–423.

Lodygensky, G.A., Rademaker, K., Zimine, S., Gex-Fabry, M., Lieftink, A.F., Lazeyras, F., Groenendaal, F., de Vries, L.S., Huppi, P.S., 2005. Structural and functional brain development after hydrocortisone treatment for neonatal chronic lung disease. Pediatrics 116, 1–7.

Lodygensky, G.A., West, T., Moravec, M.D., Back, S.A., Dikranian, K., Holtzman, D.M., Neil, J.J., 2011. Diffusion characteristics associated with neuronal injury and glial activation following hypoxia-ischemia in the immature brain. Magn. Reson. Med. 66, 839–845.

Lodygensky, G.A., West, T., Stump, M., Holtzman, D.M., Inder, T.E., Neil, J.J., 2010. In vivo MRI analysis of an inflammatory injury in the developing brain. Brain Behav. Immun. 24, 759–767.

Ma, S.F., Chen, Y.J., Zhang, J.X., Shen, L., Wang, R., Zhou, J.S., Hu, J.G., Lu, H.Z., 2015. Adoptive transfer of M2 macrophages promotes locomotor recovery in adult rats after spinal cord injury. Brain Behav. Immun. 45, 157–170.

Maalouf, E.F., Duggan, P.J., Counsell, S.J., Rutherford, M.A., Cowan, F., Azzopardi, D., Edwards, A.D., 2001. Comparison of findings on cranial ultrasound and magnetic resonance imaging in preterm infants. Pediatrics 107, 719–727.

Martinez-Biarge, M., Groenendaal, F., Kersbergen, K.J., Benders, M.J., Foti, F., Cowan, F.M., de Vries, L.S., 2016. MRI Based preterm white matter injury classification: the importance of sequential imaging in determining severity of injury. PLoS ONE 11, e0156245.

McKinstry, R.C., Miller, J.H., Snyder, A.Z., Mathur, A., Schefft, G.L., Almli, C.R., Shimony, J.S., Shiran, S.I., Neil, J.J., 2002. A prospective, longitudinal diffusion tensor imaging study of brain injury in newborns. Neurology 59, 824–833.

Merhar, S.L., Tkach, J.A., Woods, J.C., South, A.P., Wiland, E.L., Rattan, M.S., Dumoulin, C.L., Kline-Fath, B.M., 2017. Neonatal imaging using an on-site small footprint MR scanner. Pediatr. Radiol. 47, 1001–1011.

Mlynarik, V., Gambarota, G., Frenkel, H., Gruetter, R., 2006. Localized short-echo-time proton MR spectroscopy with full signal-intensity acquisition. Magn. Reson. Med. 56, 965–970.

Najac, C., Ronen, S.M., 2016. MR molecular imaging of brain cancer metabolism using hyperpolarized 13C magnetic resonance spectroscopy. Top. Magn. Reson. Imaging 25, 187–196.

Nakamura, H., Doi, M., Suzuki, T., Yoshida, Y., Hoshikawa, M., Uchida, M., Tanaka, Y., Takagi, M., Nakajima, Y., 2018. The significance of lactate and lipid peaks for predicting primary neuroepithelial tumor grade with proton MR spectroscopy. Mag. Resonance Med. Sci. 17, 238–243.

Near, J., Edden, R., Evans, C.J., Paquin, R., Harris, A., Jezzard, P., 2015. Frequency and phase drift correction of magnetic resonance spectroscopy data by spectral registration in the time domain. Magn. Reson. Med. 73, 44–50.

Nguyen, A.L.A., Ding, Y., Suffren, S., Londono, I., Luck, D., Lodygensky, G.A., 2019. The brain's kryptonite: overview of punctate white matter lesions in neonates. Int. J. Dev. Neurosci.

Nikseresht, S., Khodagholi, F., Nategh, M., Dargahi, L., 2015. RIP1 inhibition rescues from LPS-induced RIP3-mediated programmed cell death, distributed energy metabolism and spatial memory impairment. J. Mol. Neurosci. 57, 219–230.

Novikov, D.S., Fieremans, E., Jespersen, S.N., Kiselev, V.G., 2019. Quantifying brain microstructure with diffusion MRI: theory and parameter estimation. NMR Biomed. 32, e3998.

Pang, Y., Cai, Z., Rhodes, P.G., 2003. Disturbance of oligodendrocyte development, hypomyelination and white matter injury in the neonatal rat brain after intracerebral injection of lipopolysaccharide. Brain Res. Dev. Brain Res. 140, 205–214.

Pang, Y., Fan, L.W., Zheng, B., Cai, Z., Rhodes, P.G., 2006. Role of interleukin-6 in lipopolysaccharide-induced brain injury and behavioral dysfunction in neonatal rats. Neuroscience 141, 745–755.

Pardon, M.-C., Yanez Lopez, M., Yuchun, D., Marjańska, M., Prior, M., Brignell, C., Parhizkar, S., Agostini, A., Bai, L., Auer, D.P., Faas, H.M., 2016. Magnetic resonance spectroscopy discriminates the response to microglial stimulation of wild type and Alzheimer's disease models. Sci. Rep. 6, 19880.

Pavlova, M.A., Krageloh-Mann, I., 2013. Limitations on the developing preterm brain: impact of periventricular white matter lesions on brain connectivity and cognition. Brain 136, 998–1011.

Paxinos, G., Watson, C., 2007. The Rat Brain in Stereotaxic Coordinates. Academic Press/Elsevier, Amsterdam Boston.

Price, S.J., Young, A.M., Scotton, W.J., Ching, J., Mohsen, L.A., Boonzaier, N.R., Lupson, V.C., Griffiths, J.R., McLean, M.A., Larkin, T.J., 2016. Multimodal MRI can identify perfusion and metabolic changes in the invasive margin of glioblastomas. J. Magn. Reson. Imaging 43, 487–494.

Provencher, S.W., 1993. Estimation of metabolite concentrations from localized in vivo proton NMR spectra. Magn. Reson. Med. 30, 672–679.

Qu, Y., Shi, J., Tang, Y., Zhao, F., Li, S., Meng, J., Tang, J., Lin, X., Peng, X., Mu, D., 2016. MLKL inhibition attenuates hypoxia-ischemia induced neuronal damage in developing brain. Exp. Neurol. 279, 223–231.

Qu, Y., Tang, J., Wang, H., Li, S., Zhao, F., Zhang, L., Richard, Lu., Q., Mu, D.;, 2017. RIPK3 interactions with MLKL and CaMKII mediate oligodendrocytes death in the developing brain. Cell Death Dis. 8, e2629.

Ramachandra, R., Subramanian, T., 2011. Atlas of the Neonatal Rat Brain. CRC Press, Boca Raton, FL.

Raman, L., Tkac, I., Ennis, K., Georgieff, M.K., Gruetter, R., Rao, R., 2005. In vivo effect of chronic hypoxia on the neurochemical profile of the developing rat hippocampus. Brain Res. Dev. Brain Res. 156, 202–209.

Rivera, J.C., Sitaras, N., Noueihed, B., Hamel, D., Madaan, A., Zhou, T., Honore, J.C., Quiniou, C., Joyal, J.S., Hardy, P., Sennlaub, F., Lubell, W., Chemtob, S., 2013. Microglia and interleukin-1beta in ischemic retinopathy elicit microvascular degeneration through neuronal semaphorin-3A. Arterioscler. Thromb. Vasc. Biol. 33, 1881–1891.

Rosenzweig, J.M., Lei, J., Burd, I., 2014. Interleukin-1 receptor blockade in perinatal brain injury. Front. Pediatr. 2, 108.

Rygh, C.B., Wang, J., Thuen, M., Gras Navarro, A., Huuse, E.M., Thorsen, F., Poli, A., Zimmer, J., Haraldseth, O., Lie, S.A., Enger, P.O., Chekenya, M., 2014. Dynamic contrast enhanced MRI detects early response to adoptive NK cellular immunotherapy targeting the NG2 proteoglycan in a rat model of glioblastoma. PLoS ONE 9, e108414.

Sanches, E.F., Van de Looij, Y., Toulotte, A., da Silva, A.R., Romero, J., Sizonenko, S.V., 2018. Brain metabolism alterations induced by pregnancy swimming decreases neurological impairments following neonatal hypoxia-ischemia in very immature rats. Front. Neurol. 9, 480.

Savard, A., Brochu, M.E., Chevin, M., Guiraut, C., Grbic, D., Sebire, G., 2015. Neuronal self-injury mediated by IL1-beta and MMP-9 in a cerebral palsy model of severe neonatal encephalopathy induced by immune activation plus hypoxia-ischemia. J Neuroinflammation 12, 111.

Savard, A., Lavoie, K., Brochu, M.E., Grbic, D., Lepage, M., Gris, D., Sebire, G., 2013.

Involvement of neuronal IL-1beta in acquired brain lesions in a rat model of neonatal encephalopathy. J. Neuroinflammation 10, 110.

Schabitz, W.R., Fisher, M., 1995. Diffusion weighted imaging for acute cerebral infarction. Neurol. Res. 17, 270–274.

Seitz, R.J., Donnan, G.A., 2010. Role of neuroimaging in promoting long-term recovery from ischemic stroke. J. Magn. Reson. Imaging 32, 756–772.

Sharma, U., Baek, H.M., Su, M.Y., Jagannathan, N.R., 2011. In vivo (1)H MRS in the assessment of the therapeutic response of breast cancer patients. NMR Biomed. 24, 700–711.

Sijens, P.E., Levendag, P.C., Vecht, C.J., van Dijk, P., Oudkerk, M., 1996. 1H MR spectroscopy detection of lipids and lactate in metastatic brain tumors. NMR Biomed. 9, 65–71.

Simpson, R., Devenyi, G.A., Jezzard, P., Hennessy, T.J., Near, J., 2017. Advanced processing and simulation of MRS data using the FID appliance (FID-A)-An open source, MATLAB-based toolkit. Magn. Reson. Med. 77, 23–33.

Singh, K., Trivedi, R., Devi, M.M., Tripathi, R.P., Khushu, S., 2016. Longitudinal changes in the DTI measures, anti-GFAP expression and levels of serum inflammatory cytokines following mild traumatic brain injury. Exp. Neurol. 275 (Pt 3), 427–435.

Song, S.K., Sun, S.W., Ju, W.K., Lin, S.J., Cross, A.H., Neufeld, A.H., 2003. Diffusion tensor imaging detects and differentiates axon and myelin degeneration in mouse optic nerve after retinal ischemia. Neuroimage 20, 1714–1722.

Song, S.K., Sun, S.W., Ramsbottom, M.J., Chang, C., Russell, J., Cross, A.H., 2002. Dysmyelination revealed through MRI as increased radial (but unchanged axial) diffusion of water. Neuroimage 17, 1429–1436.

Song, S.K., Yoshino, J., Le, T.Q., Lin, S.J., Sun, S.W., Cross, A.H., Armstrong, R.C., 2005. Demyelination increases radial diffusivity in corpus callosum of mouse brain. Neuroimage 26, 132–140.

Stolp, H.B., Ball, G., So, P.W., Tournier, J.D., Jones, M., Thornton, C., Edwards, A.D., 2018. Voxel-wise comparisons of cellular microstructure and diffusion-MRI in mouse hippocampus using 3D Bridging of Optically-clear histology with Neuroimaging Data (3D-BOND). Sci. Rep. 8, 4011.

Sun, S.-W., Neil, J.J., Song, S.-K., 2003. Relative indices of water diffusion anisotropy are equivalent in live and formalin-fixed mouse brains. Magn. Reson. Med. 50, 743–748.

Thompson, D.K., Omizzolo, C., Adamson, C., Lee, K.J., Stargatt, R., Egan, G.F., Doyle, L.W., Inder, T.E., Anderson, P.J., 2014. Longitudinal growth and morphology of the hippocampus through childhood: impact of prematurity and implications for memory and learning. Hum. Brain Mapp. 35, 4129–4139.

Thompson, D.K., Wood, S.J., Doyle, L.W., Warfield, S.K., Lodygensky, G.A., Anderson, P.J., Egan, G.F., Inder, T.E., 2008. Neonate hippocampal volumes: prematurity, perinatal predictors, and 2-year outcome. Ann. Neurol. 63, 642–651.

Tkac, I., Keene, C.D., Pfeuffer, J., Low, W.C., Gruetter, R., 2001. Metabolic changes in quinolinic acid-lesioned rat striatum detected non-invasively by in vivo (1)H NMR spectroscopy. J. Neurosci. Res. 66, 891–898.

Tkach, J.A., Merhar, S.L., Kline-Fath, B.M., Pratt, R.G., Loew, W.M., Daniels, B.R., Giaquinto, R.O., Rattan, M.S., Jones, B.V., Taylor, M.D., Tiefermann, J.M., Tully, L.M., Murphy, E.C., Wolf-Severs, R.N., LaRuffa, A.A., Dumoulin, C.L., 2013. MRI in the neonatal ICU: initial experience using a small-footprint 1.5-T system. Am. J. Roentgenol. 202, W95–W105.

Toussaint, M., Pinel, S., Auger, F., Durieux, N., Thomassin, M., Thomas, E., Moussaron, A., Meng, D., Plenat, F., Amouroux, M., Bastogne, T., Frochot, C., Tillement, O., Lux, F.,

Barberi-Heyob, M., 2017. Proton MR spectroscopy and diffusion MR imaging monitoring to predict tumor response to interstitial photodynamic therapy for glioblastoma. Theranostics 7, 436–451.

Tuor, U.I., Morgunov, M., Sule, M., Qiao, M., Clark, D., Rushforth, D., Foniok, T., Kirton, A., 2014. Cellular correlates of longitudinal diffusion tensor imaging of axonal degeneration following hypoxic–ischemic cerebral infarction in neonatal rats. NeuroImage: Clinical 6, 32–42.

van de Looij, Y., Chatagner, A., Huppi, P.S., Gruetter, R., Sizonenko, S.V., 2011. Longitudinal MR assessment of hypoxic ischemic injury in the immature rat brain. Magn. Reson. Med. 65, 305–312.

van de Looij, Y., Chatagner, A., Quairiaux, C., Gruetter, R., Huppi, P.S., Sizonenko, S.V., 2014a. Multi-modal assessment of long-term erythropoietin treatment after neonatal hypoxic-ischemic injury in rat brain. PLoS ONE 9, e95643.

van de Looij, Y., Ginet, V., Chatagner, A., Toulotte, A., Somm, E., Huppi, P.S., Sizonenko, S.V., 2014b. Lactoferrin during lactation protects the immature hypoxic-ischemic rat brain. Ann. Clin. Transl. Neurol. 1, 955–967.

Volpe, J.J., 2009. Brain injury in premature infants: a complex amalgam of destructive and developmental disturbances. Lancet Neurol. 8, 110–124.

Wang, K.C., Fan, L.W., Kaizaki, A., Pang, Y., Cai, Z., Tien, L.T., 2013. Neonatal lipopolysaccharide exposure induces long-lasting learning impairment, less anxiety-like response and hippocampal injury in adult rats. Neuroscience 234, 146–157.

Wang, W.T., Lee, P., Dong, Y., Yeh, H.W., Kim, J., Weiner, C.P., Brooks, W.M., Choi, I.Y., 2016. In vivo neurochemical characterization of developing guinea pigs and the effect of chronic fetal hypoxia. Neurochem. Res. 41, 1831–1843.

Winklewski, P.J., Sabisz, A., Naumczyk, P., Jodzio, K., Szurowska, E., Szarmach, A., 2018. Understanding the physiopathology behind axial and radial diffusivity changes—What do we know? Front. Neurol. 9.

Xie, M., Tobin, J.E., Budde, M.D., Chen, C.I., Trinkaus, K., Cross, A.H., McDaniel, D.P., Song, S.K., Armstrong, R.C., 2010. Rostrocaudal analysis of corpus callosum demyelination and axon damage across disease stages refines diffusion tensor imaging correlations with pathological features. J. Neuropathol. Exp. Neurol. 69, 704–716.

Xu, S., Zhuo, J., Racz, J., Shi, D., Roys, S., Fiskum, G., Gullapalli, R., 2011. Early microstructural and metabolic changes following controlled cortical impact injury in rat: a magnetic resonance imaging and spectroscopy study. J. Neurotrauma 28, 2091–2102.

Yamasaki, F., Takayasu, T., Nosaka, R., Amatya, V.J., Doskaliyev, A., Akiyama, Y., Tominaga, A., Takeshima, Y., Sugiyama, K., Kurisu, K., 2015. Magnetic resonance spectroscopy detection of high lipid levels in intraaxial tumors without central necrosis: a characteristic of malignant lymphoma. J. Neurosurg. 122, 1370–1379.

Zahr, N.M., Mayer, D., Rohlfing, T., Sullivan, E.V., Pfefferbaum, A., 2014. Imaging neuroinflammation? A perspective from MR spectroscopy. Brain Pathol. (Zurich, Switzerland) 24, 654–664.

Zhang, J., Aggarwal, M., Mori, S., 2012. Structural insights into the rodent CNS via diffusion tensor imaging. Trends Neurosci. 35, 412–421.

Zhao, M., Lu, L., Lei, S., Chai, H., Wu, S., Tang, X., Bao, Q., Chen, L., Wu, W., Liu, X., 2016. Inhibition of receptor interacting protein kinases attenuates cardiomyocyte hypertrophy induced by palmitic acid. Oxid Med Cell Longev 2016, 1451676.

Zhuo, J., Xu, S., Proctor, J.L., Mullins, R.J., Simon, J.Z., Fiskum, G., Gullapalli, R.P., 2012. Diffusion kurtosis as an in vivo imaging marker for reactive astrogliosis in traumatic brain injury. Neuroimage 59, 467–477.